AAPG BULLETIN

Analysis of fault damage-zones using 3D seismic coherence in the Anadarko Basin, Oklahoma

Zonghu Liao, Hui Liu, Brett M. Carpenter, Kurt J. Marfurt, and Ze'ev Reches

AAPG Bulletin published online 21 December 2018
doi: 10.1306/12191814134 17207

Cite as: Liao, Z., H. Liu, B. M. Carpenter, K. J. Marfurt, and Z. Reches, Analysis of fault damage-zones using 3D seismic coherence in the Anadarko Basin, Oklahoma, *(in press; preliminary version published online Ahead of Print* 21 December 2018*):* AAPG Bulletin, doi: 10.1306/12191814134 17207.

Analysis of fault damage-zones using 3D seismic coherence in the Anadarko Basin, Oklahoma

Zonghu Liao[a*], Hui Liu[a], Brett M. Carpenter[b], Kurt J. Marfurt[b], and Ze'ev Reches[b]

[a]College of Geosciences, China University of Petroleum, Beijing, 102249, China

[b]School of Geology and Geophysics, University of Oklahoma, Norman, OK, 73019

*Corresponding author: zonghuliao@163.com, +86-132-6018-8886

ABSTRACT

Fault damage-zones may significantly affect subsurface fluid migration and the development of unconventional resources. Most analyses of fault damage-zones are based on direct field observations, and we expand these analyses to the subsurface by investigating the damage-zone structure of a 32-km (~10^5 ft) long right-lateral strike-slip fault in Oklahoma. We used the 3D seismic attribute of coherence to first define its regional and background levels, and then evaluated the damage-zone dimensions at multiple sites. We found damage-zone thickness of ~1600m (5,300 ft) at a segment that is dominated by subsidiary faults, and it is slightly thicker at a segment with a pull-apart basin. The damage-zone intensity decays exponentially with distance from the fault core, in agreement with field observations and distribution of seismic events. The coherence map displays a strong asymmetry of the damage-zone between the two sides of the 3D fault, which is related to the subsidiary structures of the fault-zone. We discuss the effects of heterogeneous stress field on damage-zone evolution through the detected subsidiary structures. It appears that seismic coherence is an effective tool for subsurface characterization of fault damage-zones.

INTRODUCTION

FAULT-ZONE STRUCTURE

Field analyses of fault-zones has revealed three primary components: fault core, damage-zone, and protolith (Figure 1) (Caine et al., 1996; Sagy et al. 2001; Kim et al., 2004; Savage and Brodsky, 2011). The fault core is a discrete, quasi-tabular shear zone, comprised of gouge layers that accommodates most fault displacement. If the fault is composed of strands with several anastomosing segments, its core could be up to meters thick (e.g., Faulkner et al., 2010; Savage and Brodsky, 2011). The fault core could be a sealing zone with thick clay bodies (e.g. Billi et al., 2003), a permeable conduit (e.g. Caine et al., 1996), or both, depending on the fault's state in its seismic cycle (e.g. Sibson, 1990). The damage-zone is constituted of fractured, brecciated, and pulverized rocks derived from the protolith and are generally confined to a zone on the scale of a kilometer between the fault core and intact protolith (Sibson, 2003; Rempe et al., 2013; Busetti et al., 2012). The fracture sets within the damage-zone often provide a high permeability conduit for fluid flow (Billi et al., 2003). The fault core and damage-zone may vary along strike, owing to fault-related diagenesis, segmentation and evolution (Laubach et al., 2014). The structural complexity within the damage-zones, and particularly the distribution and openness of its fracture networks, can significantly affect the migration, accumulation and leakage of subsurface fluids (e.g., Caine et al., 1996; Faulkner et al., 2010; Ellis et al., 2012) and earthquake rupture characteristics (e.g., Weng et al., 2016).

Characterization of the structure of a subsurface fault zone, without borehole data, can be done only indirectly because fracture networks are invisible to seismic data. The properties of subsurface fault patterns, including geometry and internal architecture, can be determined, for example, by using seismic attributes (Chopra and Marfurt, 2007). Application of seismic mapping to a submarine fold thrust system can detect structural deformation by recognition of reduced signal through volumes (Iacopini and Butler, 2011; Iacopini et al., 2012). The concept of a seismic distortion zone enhanced the understanding of the associated damage of a thrust system at seismic scales. This seismic characterization method is further used for fault structure and its surrounding deformation that is defined as a seismic disturbance zone (Iacopini et al., 2016). Even though the fracture networks are invisible at seismic scale, their cumulative effects could be detected as distortion of the signal (Chopra and Marfurt, 2010; Li et al., 2015). Numerical simulations of synthetic fault models and associated seismic responses shows the potential to characterize the damage zones using seismic attributes and seismic tomography, as presented by Botter et al. (2016, 2017). Their workflow provides information on fault structure at different seismic resolutions, through the seismic images determined by the discrete element modeling.

The present study utilizes 3D seismic attributes for the analysis of damage and splays of a large, subsurface strike-slip fault in Oklahoma. It is demonstrated that the utilized seismic approach can reveal the dimensions and shapes of damage-zones with indications of the deformation intensity. We further show that the detected subsurface damage-zone display similar scaling relation to well documented field observations.

DAMAGE-ZONE DIMENSION

It is commonly observed that the intensity of fracturing and deformation within a fault damage-zone decays with distance from the fault core toward the protolith (e.g. Caine et al., 1996; Sagy et al. 2001; Katz et al., 2003; Savage and Brodsky, 2011; Rempe et al., 2013). Sagy et al. (2001) analyzed a system of joints within dolomite layers close to a large normal fault of the Dead Sea basin. The joint density, reported by the FSR (Fracture-Spacing-Ratio) = layer thickness/joint spacing, decreased significantly from FSR = 28 close to the fault core to a background value of 2-3 at ~100 m (330 ft) away from the core (Figure 2a). Wilson et al. (2003) analyzed the brittle deformation around the Punchbowl fault in California. They found that the density of subsidiary fractures in the sandstone decreases from about ~90 fractures/m at the sub-fault core, to a regional background of ~20 fractures/m at about 10 m (33 ft) distance (Figure 2b). In general, the observed damage decay can be fit by a power function or an exponential function (Figure 2), for example, the fracture density (*D*) decays as fault-normal distance (*x*):

$$D = \mathrm{a}\, e^{-\mathrm{b}x}$$

where a and b are constants that reflect physical properties related to the layer thickness or brittleness of the rock (Cowie et al., 1995).

Determination of the dimension of subsurface damage-zones is challenging. Peng et al. (2003) used synthetic wave modeling to determine a thickness of ~100 m (330 ft) for a shallow fault in Landers, California. They found that the fault-zone has a ~50% decrease in seismic velocity compared to the surrounding protolith. Powers and Jordan (2010) analyzed the variation of seismicity rate around right-lateral strike-slip faults in California (Figure 2c). In the fault core, the number of seismic events is ~120 per km (~3,300 ft) normal to the fault, and this seismicity rate decayed to 20/km (~66,000 ft) at a distance of 10 km (~33,000 ft) by a power-law relationship with distance from the fault core. Their estimates of thicknesses of the damage-zones ranged from 120 m (~400 ft) to 440 m (~1400 ft) along Elsinore-Temecula segment of the southern San Andreas California fault system. Valoroso et al., (2014) used high-resolution earthquake locations to evaluate the damage zone of the L'Aquila normal fault, Italy. They found damage zone thicknesses ranging 0.5 km (~1,600 ft) to 1.5 km (~5,000 ft) with damage intensity decaying at an exponential rate with distance from the fault core, which is in general agreement with field observations. Additional information can be derived from borehole logs. For example, the drilling across the San-Andreas fault near Parkfield, revealed a 200 m (~660 ft) thick damage-zone based on reduced seismic velocities (e.g. Zoback et al., 2011).

DAMAGE-ZONE OF A SUBSURFACE STRIKE-SLIP FAULT: 3D SEISMIC ANALYSIS

APPROACH AND OBSERVATIONS

We investigate the damage-zone of the El Reno fault (ERF), a 32 km (~10^5 ft) long, right-lateral, strike-slip fault in the Anadarko Basin, Oklahoma. The analysis utilizes the 3D seismic attribute "coherence" which is defined as the energy of the coherent part of seismic traces divided by the average acoustic energy of the input seismic traces (Chopra and Marfurt, 2007; Chopra and Marfurt, 2010). This attribute is commonly used to identify lateral discontinuities, under the premise that its low values indicate discontinuities in layers, for example usage to detect faults and damage zones in the subsurface (e.g., Chopra and Marfurt, 2007; Liao et al., 2013; Iacopini et al., 2016; Botter et al., 2017). Here, we focus on utilizing coherence for characterization of seismic scale damage-zone in 3D to demonstrate the practical effectiveness of this attribute for damage-zone analysis for an onshore case of a large fault in an oil province.

The study area is in central-west Oklahoma (inset Figure 3) where the Devonian Woodford Shale was deposited in the Anadarko, Arkoma, and Ardmore Basins (Paxton et. al., 2006; Cardott, 2008) during a global sea-level transgression (Johnson, 1988; Lambert, 1993). The Woodford Shale is an important petroleum source rock in the United States midcontinent, characterized as a laminated unit with alternating brittle and ductile layers (Slatt et al., 2010). The quartz- and calcite-rich brittle layers are fractured by layer-perpendicular open fractures

(Bernal et al., 2012). Gale et al. (2014) observed widely distributed small fractures with heights < 3 cm in thin chert layers of the Woodford.

The seismic data analyzed here were collected in 2012, and it includes nine narrow azimuth surveys that were reprocessed and prestack time migrated using a single datum and the same bin size (33.5 by 33.5 m or 110 ft by 110 ft). The frequency ranged from 10 to 60 Hz yielding the increased impedance as positive amplitude. The coherence volume calculations followed the procedure of Marfurt and Rich (2010).

The general features of the study area are displayed by a time structure map co-rendered with a map-based extraction from the seismic coherence volume at the Woodford Shale level (Figure 3b). The dark zone (within the red box) indicates a north-south fault in the eastern part of the area that is the El Reno fault (ERF). Our previous study (Liao et al., 2013) indicated that the ERF is a right-lateral strike-slip fault based on two distinguishing features: 1) it is a vertical fault with several sub-parallel vertical segments (Liao et al., 2013), which is typical feature of strike-slip faults (Harding, 1985; Christie-Blick and Biddle, 1985); and 2) the relatively small vertical throw (~80 m or 260 ft) is in contrast to the large fault length of 32 km (~10^5 ft or 20 mi)), and vertical extent of at least 900 m (~3,000 ft) (Figure 4).

The structure of the ERF at its intersection with the top of the Woodford Shale is displayed by the coherence map (Figure 3). The structure includes a system of folds and flexures that are most intense within a zone around the primary fault zone (Liao et al., 2017). We interpret this structure as the damage-zone of ERF, and evaluate its thickness in 11 horizontal, fault-normal sections of coherence. These sections are spaced at ~1500 m (5,000 ft) intervals along the ERF (marked ‘C’ in Figure 3). The seismic amplitude and coherence section samples are presented in Figure 4, and the coherence profiles are displayed in Figure 5.

It has been shown that between the Rayleigh limit and distinctive seismic response scale, seismic attributes could be interpreted to track structure details by an image processing procedure (Liao et al., 2013; Iacopini et al., 2016). Figure 4 displays vertical sections of amplitude (Figure 4 a, b) and coherence (Figure 4 c, d) along line C2 and C8 (defined in Figure 3) that are perpendicular to ERF. These sections reveal a few discrete vertical zones, with the ERF (red, dashed box) as the most prominent zone. The amplitude signals are strongly disturbed around the vertical fault zones, which is enhanced by the low coherence maps. The vertical fault zones are comprised of several vertical segments that become wider with depth. These seismic disturbance zones are analyzed here as the seismic damage zone of two structural types (type 1 in Figure 4a, c, and type 2 in Figure 4b, d) along the strike-slip fault. The internal character of these structural types is discussed below.

The profiles display three general zones of coherence intensity (Figure 5; note inverted scale of the coherence): 1. Zones of high coherence, > 0.9, observed away from the ERF; 2. Zones of intermediate coherence, 0.8-0.9, within the ERF zone (gray in Figure 5); and 3. A zone of low coherence, 0.4-0.8, within the ERF (pink in Figure 5). The coherence levels in 3D-seismic analysis indicate the intensity of structural disturbance and discontinuities (Chopra and Marfurt, 2010). As fracturing and faulting disturb the continuity of geologic features, we regard the three coherence zones of Figure 5 as indicating three levels of damage intensity. The high coherence zone is the protolith zone away from the fault, the intermediate level zone is the damage-zone, and the low coherence level zone is the fault core that is most intensely damaged, which is defined here as the ‘seismic fault core’. We apply this interpreted zonation in the synthesis below.

We further explored the validity of the above interpretation of damage-zones by plotting the root mean square (RMS) of the seismic amplitude along the same profiles of Figure 5. We regard the amplitude RMS as a proxy for the reduction of the seismic intensity due to damage and found that the amplitude RMS at the Woodford Formation horizon corresponds well to the coherency plots of Figure 5. Yet, while the coherency sections revealed both fault core (pink) and damage zone (grey), the amplitude RMS plots did not display the core (Figure 6).

SYNTHESIS

We noted that the width of the damage-zone (gray in Figure 5) is asymmetric with respect to the seismic core-zone (pink in Figure 5), and based on this asymmetry, we separated the coherence profiles into two types. Type 1, which includes profiles C1-C7 (Figure 5a), displays a strong asymmetry in which the damage-zone is ~1,100 m (3,600 ft) wide in the western block of ERF and only ~75 m (250 ft) wide in the eastern block. A core-zone (pink), of ~400 m (1312 ft) width, separates the two blocks. Type 2, which includes profiles C6-C11 (Figure 5b), has a ~1,600 m (5,400 ft) thick damage-zone (coherence < 0.9), that includes a central core-zone of ~500 m (1,600 ft) width. This type displays a gentler asymmetry with a western damage-zone of ~760 m (2,500 ft) width, and an eastern damage-zone of ~380 m (1,200 ft) width. These types correspond to different structural styles that were recognized by Liao et al., (2017). Type 1 corresponds to ERF segments with multiple, subsidiary Riedel faults trending at 15°-30° with respect to the main trend (red dash lines illustrated R faults in Figure 3a, or refer to Liao et al., 2017). Type 2, on the other hand, is associated with segments of ERF with pull-apart basin (e.g., area between profiles C8-C9 in Figure 3).

The dimensions and shapes of the identified coherence zones (Figure 5), which we interpret as damage-zones, can be compared to equivalent features of exposed damage-zones. First, both types displayed asymmetry of damage-zone width with respect to the seismic fault-core (Figure 5), and similar asymmetry has been observed in field cases and derived in theoretical models. Dor et al., (2006) found a systematic asymmetry of damage and pulverization distribution along multiple fault segments of the southern part of the San Andreas system in California. The pulverized rocks along these faults were typically associated with fault segments that separate rock bodies of different elastic properties. This association suggests that the asymmetric damage is related to preferential rupture propagation during earthquakes (Ben-Zion and Shi, 2005; Xu et al., 2012b; Ampuero and Mao, 2016). It was modeled in rupture simulations of bi-material faults that this preferred propagation direction would lead to strong strain asymmetry between the two sides of the fault (Cochard and Rice, 2000; Shi and Ben-Zion, 2006; Dalguer and Day, 2009; Ampuero and Mao, 2016).

To examine depth variations of the damage-zones, we plotted a sequence of coherence profiles at 50 ms time intervals that are similar to the single depth sections of Figure 5. The damage zones, marked grey in Figure 7 for type 1 (a) and type 2 (b), are wider (>1000 m or 3280 ft) within the central part of the fault (e.g., intervals 1950-2000 ms in Figure 7a), and are thinner upward and downward (e.g., 1800ms or 2150ms, Figure 7a). Similar width variations can be observed for a type 2 segment (Figure 7b). This reduction of damage-zone width from fault center towards its margins, fits the well-documented observation that the largest displacement along a fault which is, in general, within its central region (Walsh and Watterson, 1987; Cowie and Scholz, 1992). However, the change in damage zone width from shallow to deep could be possibly influenced by differences in the connectivity of the various strands in subsurface, which is not to be discussed in this paper.

We further compare the geometry of the coherence zones to damage distribution in field studies. Figure 8a shows the normalized density of fractures as a function of normalized distance from the fault zone for the aforementioned three examples using seismic data (Powers and Jordan, 2010) and outcrop data (Sagy et al., 2001; Wilson et al., 2003). The curves of normalized density fit well the above exponential model (equation 1) with slightly different coefficients, a and b, that reflect the fault lithology and geometry. Figure 8b shows the normalized coherence of the two fault blocks in type 1 (average values of C1-C7), displaying an exponential decay of the coherence as a function of increasing distance from the core. Within a wider damage-zone, the deformation consists of subsidiary faults indicated by two pulses of coherence values (Figure 8c). Similar patterns of coherence (average of C6-C11) are observed in type 2 (Figure 8de). Figure 8e illustrate the extreme coherence anomaly of the eastern fault block of the pull-apart basin. These two types indicate that the thickness of a damage-zone covers a distance of two orders of magnitude.

DISCUSSION

The damage-zone of a fault can develop by various mechanisms. For example, earthquake propagation along a fault radiates seismic waves that could damage the surrounding blocks (e.g. Andrews, 1994, Dor et al., 2006). The intensity of this damage was analyzed and simulated based on the stress distribution during rupture and fault properties (Ben-Zion and Ampuero, 2009; Xu et al. 2012b), and the analyses showed that the damage-zone thickness depends primarily on fault depth, pre-earthquake stresses, and the intensity of stress drop during rupture (Ampuero and Mao, 2017). For example, a 15 km (~5×10^4 ft) deep strike-slip fault is expected to generate a ~400 m (1300 ft) thick damage zone for typical crustal conditions (Ampuero and Mao, 2017). The vertical extent of the present El Reno fault is about 900 m (~3,000 ft) and thus the expected damage-zone due to earthquake rupture is less than 100 m. As our analysis revealed a much thicker damage-zone (~ 1600 m or 5,000 ft), we propose that most of the observed damage is associated with the following evolution of fault growth. First, the early stages of fault evolution is characterized by development of multiple fractures and small faults that precede the localized slip in the core-zone, due partly to the merger and coalescence of these smaller structures (e.g., Reches and Lockner, 1994; Heesakkers et al., 2011a, b). A large strike slip fault, like the present El Reno fault, evolves over extended time, and may develop a complex damage distribution that generates a wide zone. Experimental works have shown that strike slip faults typically initiate as a wide, simple-shear zone with multiple secondary structures (Riedel shears, P shears), that eventually merge into a complex fault-zone (Naylor et al., 1986; Reches 1988; Liao et al., 2013). This process forms a wide damage-zone that continues to deform internally due to the non-planar, intersecting relation of the coalesced secondary faults. Such evolution may lead to a rough fault core (Sagy et al., 2001), and the slip along such a rough fault generates a heterogeneous stress field comparable to the scale of the roughness (Dieterich and Smith, 2009; Powers and Jordan, 2010). Figure 9 displays a model calculation of the stress distribution at the proximity of a rough strike-slip fault (Chester et al., 2005). This stress field leads to further damage by branching of multiple secondary faults and general fracturing, particularly in the more tensile area (Reches, 1988), as well as multiple short folds and flexures. The ERF, studied here, is likely to be at a mature stage of its development, and we argue that the above processes prevailed during its activity forming the damage-zones with reduced seismic coherence.

Conclusions

The present analysis of the damage-zone of El Reno fault in Oklahoma by using seismic attributes led to the following conclusions:

1. The analysis shows the effectiveness of using the 3D seismic attribute of coherence for characterization of the structural features of large fault-zones.
2. The thickness variations of the damage-zone of the El Reno segments fit an exponential decay with distance from the fault core. This scaled decay function agrees with field observations over different scales, and may be applied to characterize damage zone dimensions in the subsurface.
3. It is suggested that the pattern and scale of damage-zone thickness is controlled by the secondary structures that develop during fault evolution.

ACKNOWLEDGMENTS

The authors would like to thank CGG for providing a license to their 3D seismic data; the sponsors of the Attribute Assisted Seismic Processing and Interpretation (AASPI), University of Oklahoma and N. Gupta for their help. Additional support funding was provided by Strategic Priority Research Program of the Chinese Academy of Sciences (No. XDA14010306), the National Natural Science Foundation of China (NSFC) (No. 41604036), and NSFC for Major projects (U1663203), and Science Foundation of China University of Petroleum, Beijing (No. 2462014YJRC013). We would like to thank S. Laubach, B. Katz, D. Iacopini, T. Allwardt, F. Whitehurst, and two anonymous reviewers for their thoughtful and detailed reviews, which helped improve this manuscript.

REFERENCE:

Al-Dossary, S., and K. J. Marfurt, 2006, 3D volumetric multispectral estimates of reflector curvature and rotation: Geophysics, v. 71, p. 41-51.

Ampuero, J. P., and X. Mao, 2016, Scaling between fault length, damaged zone thickness and width of secondary fault fans derived from fracture mechanics: EGU General Assembly Conference, Vienna Austria.

Ampuero, J. P., and X. Mao, 2017, Upper limit on damage zone thickness controlled by seismogenic depth: AGU monograph, p. 243-254.

Andrews, D. J., 1994, Fault geometry and earthquake mechanics: Annals of Geophysics, v. 37, p. 6.

Ben-Zion, Y., and Z. Shi, 2005, Dynamic rupture on a material interface with spontaneous generation of plastic strain in the bulk: Earth and Planetary Science Letters, v. 236, p. 486–496.

Ben-Zion, Y., and J. P. Ampuero, 2009, Seismic radiation from regions sustaining material damage: Geophysical Journal International, v. 178, no. 3, p. 1351-1356.

Bernal, A. S., L. C. Mayorga, A. G. Prada, and R. M. Slatt, 2012, Geological characterization of the Woodford Shale, McAlester Cemetery Quarry, Oklahoma: Shale Shaker, v. 63, no. 3, p. 202-212.

Billi, A., F. Salvini, and F. Storti, 2003, The damage zone-fault core transition in carbonate rocks: implications for fault growth, structure and permeability: Journal of Structural Geology, v. 25, p. 1779-1794.

Botter, C., N. Cardozo, S. Hardy, I. Lecomte, G. Paton, and A. Escalona, 2016, Seismic characterization of fault damage in 3D using mechanical and seismic modelling: Marine and Petroleum Geology, v. 77, p. 973-990.

Botter, C., N. Cardozo, D. Qu, J. Tveranger, and D. Kolyukhin, 2017, Seismic characterization of fault facies models: Interpretation, v. 5, p. 1-53.

Busetti, S., K. Mish, P. Hennings, and Z. Reches, 2012, Damage and plastic deformation of reservoir rocks: Part 2. Propagation of a hydraulic fracture: AAPG bulletin, v. 96, p. 1711-1732.

Caine, J. S., J. P. Evans, and C. B. Forster, 1996, Fault zone architecture and permeability structure: Geology, v. 24, p. 1025–1028.

Cardott, B., 2008, Overview of Woodford gas-shale play of Oklahoma, US: AAPG Annual Convention and Exhibition, http://ogs.ou.edu/pdf/AAPG08woodford.pdf.

Chester, J. S., F. M. Chester, and A. K. Kronenberg, 2005, Fracture surface energy of the Punchbowl fault, San Andreas system: Nature, v. 437, p. 133-136.

Chopra, S., and K. J. Marfurt, 2007, Seismic attributes for prospect identification and reservoir characterization: Houston, USA, SEG publisher, SEG Geophysical Developments Series, no. 11.

Chopra, S. and K. J. Marfurt, 2010, Interpreting fractures through 3-D seismic discontinuity attributes and their visualization: CSEG Recorder, v. 34, no. 8.

Christie-Blick, N. and K. T. Biddle, 1985, Deformation and basin formation along strike-slip faults, in Biddle, K. T. and N. Christie-Blick, eds., Strike-slip deformation, basin formation, and sedimentation: SEPM Special Publications, v. 37, p. 1-34.

Cochard, A., and J. R. Rice, 2000, Fault rupture between dissimilar materials: Illposedness, regularization, and slip-pulse response: Journal of Geophysical Research Atmospheres, v. 105, B11, p. 25891-25907.

Cowie, P. A., & Scholz, C. H., 1992. Displacement-length scaling relationship for faults: data synthesis and discussion. Journal of Structural Geology, 14, 1149-1156.

Cowie, P. A., D. Sornette, and C. Vanneste, 1995, Multifractal scaling properties of a growing fault population: Geophysical Journal International, v. 122, p. 457-469.

Dalguer, L.A., and S. M. Day, 2009, Asymmetric rupture of large aspect-ratio faults at bimaterial interface in 3D: Geophysical Research Letters, v. 36, p. 195-215.

Dieterich, J. H., and D. E. Smith, 2009, Nonplanar faults: mechanics of slip and off-fault damage: Pure and Applied Geophysics, v. 166, p. 1799-1815.

Dor, O., T. K. Rockwell, and Y. Ben-Zion, 2006, Geological observations of damage asymmetry in the structure of the San Jacinto, San Andreas and Punchbowl faults in Southern

California: A possible indicator for preferred rupture propagation direction: Pure and Applied Geophysics, v. 163, p. 301-349.

Ellis, M. A., S. E. Laubach, P. Eichhubl, J. E. Olson and P. Hargrove, 2012, Fracture development and diagenesis of Torridon Group Applecross Formation, near An Teallach, NW Scotland millennia of brittle deformation resilience: Journal of the Geological Society, London, v. 169, no. 3, p. 297-310.

Faulkner, D. R., C. A. L. Jackson, R. J. Lunn, R. W. Schlische, Z. K. Shipton, C. A. J. Wibberley, and M. O. Withjack, 2010, A review of recent developments concerning the structure, mechanics and fluid flow properties of fault zones: Journal of Structural Geology, v. 32, p. 1557-1575.

Gale, J. F., S.E. Laubach, J.E. Olson, P. Eichhubl, A. Fall, 2014, Natural fractures in shale: A review and new observations: AAPG Bulletin, v. 98, no. 11, p. 2165-2216.

Harding, T. P., 1974, Petroleum traps associated with wrench fault: AAPG Bulletin, v. 58, no. 7, p. 1290-1304.

Harding, T. P., 1985, Seismic characteristics and identification of negative flower structures, positive flower structures and positive structural inversion: AAPG Bulletin, v. 69, no. 4, p. 1016-1058.

Heesakkers, V., S. Murphy, and Z. Reches, 2011a, Earthquake Rupture at Focal Depth, Part I: Structure and Rupture of the Pretorius Fault, TauTona Mine, South Africa: Pure and Applied Geophysics, v. 168, p. 2395-2425.

Heesakkers, V., S. Murphy, D. A. Lockner, and Z. Reches, 2011b, Earthquake Rupture at Focal Depth, Part II: Mechanics of the 2004 M2.2 Earthquake Along the Pretorius Fault, TauTona Mine, South Africa: Pure and Applied Geophysics, v. 168, p. 2427-2449.

Iacopini, D., and R.W.H. Butler, 2011, Imaging deformation in submarine thrust belts using seismic attributes: Earth and Planetary Science Letters, v. 302, p. 414–422.

Iacopini, D., R.W.H., Butler, and S. Purves, 2012, Seismic imaging of thrust faults and structural damage visualization workflow for deepwater thrust belts: First Break, v. 30, p. 39-46.

Iacopini, D., R.W.H. Butler, S. Purves, N. McArdle, and N. De Freslon, 2016. Exploring the seismic expression of fault zones in 3D sesimci volume: Journal of structural geology, v. 89, p. 54-73.

Johnson, K. S., 1988, Geologic evolution of the Anadarko basin, in K. S. Johnson, ed., Anadarko basin Symposium: Circular 90, Oklahoma Geological Survey, p. 3-12.

Katz, O., Z. Reches, and G. Baer., 2003, Faults and their associated host rock deformation: Part I. Structure of small faults in a quartz–syenite body, southern Israel. Journal of Structural Geology, v. 25, p. 1675-1689.

Kim, Y. S., D. C. P. Peacock, and D. J. Sanderson, 2004, Fault damage zones: Journal of Structural Geology, v. 26, p. 503-517.

Lambert, M. W., 1993, Internal stratigraphy and organic facies of the Devonian-Mississippian Chattanooga (Woodford) Shale in Oklahoma and Kansas: Source rocks in a sequence stratigraphic framework: AAPG Studies in Geology, v. 37, p.163–176.

Laubach, S.E., P. Eichhubl, P. Hargrove, M.A. Ellis, J.N. Hooker, 2014, Fault core and damage zone fracture attributes vary along strike owing to interaction of fracture growth, quartz accumulation, and differing sandstone composition: Journal of Structural Geology, v. 68, p. 207-226.

Li, F., T. Zhao, T. Lin, and K. J. Marfurt, 2015, Fracture characterization based on attenuation estimation from seismic reflection data using well-log-based localized spectral correction: Unconventional Resources Technology Conference (URTeC),) DOI 10.15530/urtec-2015-2152510.

Liao, Z., Z. Reches, K. J. Marfurt, and N. Gupta, 2013, Characterizing a fault-zone and associated fractures using lab experiments and attribute-based seismic analysis: an example from Woodford Shale: 83rd Annual International Meeting of the SEG Expanded Abstracts, p. 1416-1420.

Liao, Z., H. Liu, Z. Jiang, K. J. Marfurt, and Z. Reches, 2017, Fault damage zone at subsurface: a case study using 3D seismic attributes and a clay model analogue for the Anadarko Basin, Oklahoma: Interpretation, v. 5, p. 143-150.

Marfurt, K. J., and J. Rich, 2010, Beyond curvature – Volumetric estimation of reflector rotation and convergence: 80th Annual International Meeting of the SEG, Expanded Abstracts, p. 1467-1472.

Marone, C., and C. H. Scholz, 1989, Particle-size distribution and microstructure within simulated fault gouge: Journal of Structural Geology, v. 11, no. 7, p. 799-814.

Naylor, M. A., G. Mandl, and C. H. K. Supesteun, 1986, Fault geometries in basement-induced wrench faulting under different initial stress states, Journal of Structural Geology, v. 8, p. 737-752.

Paxton, S. T., A. M. Cruse, and A. M. Krystyniak, 2006, Detailed fingerprints of global sea-level change revealed in Upper Devonian / Mississippian Woodford Shale of south-central Oklahoma: AAPG Annual Meeting.

Peng, Z., Y. Ben-Zion, A. J. Michael, and L. Zhu, 2003, Quantitative analysis of seismic fault zone waves in the rupture zone of the 1992 Landers, California, earthquake: evidence for a shallow trapping structure: Geophysical Journal International, v. 155, p. 1021-1041.

Powers, P. M., and T. H. Jordan, 2010, Distribution of seismicity across strike-slip faults in California: Journal of Geophysical Research, v. 115, no. B05, p. 3040.

Reches, Z., 1988, Evolution of fault patterns in clay experiments: Tectonophysics, v. 145, no. 1, p. 141-156.

Reches, Z., and D. A. Lockner, 1994, Nucleation and growth of faults in brittle rocks: Journal of Geophysical Research Atmospheres, v. 99, p. 18159-18173.Rempe, M., T. Mitchell, J. Renner, S. Nippress, Y. Ben-Zion, and T. Rockwell, 2013, Damage and seismic velocity structure of pulverized rocks near the San Andreas Fault: Journal of Geophysical Research, v. 118, p. 2813-2831.

Savage, H. M., and E. E. Brodsky, 2011, Collateral damage: Evolution with displacement of fracture distribution and secondary fault strands in fault damage zones: Journal of Geophysical Research, v. 116, no. B03405, p. 428-452.

Sagy, A., Z. Reches, and I. Roman, 2001, Dynamic fracturing: field and experimental observations: Journal of Structural Geology, v. 23, p. 1223-1239.

Sibson, R. H., 1990, Conditions for fault-valve behaviour: Geological Society London Special Publications, v. 54, p. 15-28.

Sibson, R. H., 2003, Thickness of the seismic slip zone: Bulletin of the Seismological Society of America, v. 93, no. 3, p. 1169-1178.

Slatt, R. M., R. Portas, N. Buckner, Y. Abousleiman, N. M. O'Borien, R. Sierra, P. Philp, A. Miceli-Romero, R. Davis, and T. Wawrzyniec, 2012, Outcrop−behind outcrop (quarry): Multiscale characterization of the Woodford gas shale, Oklahoma: AAPG Memoir 97, p. 382-402.

Shi, Z., and B. Yehuda, 2006, Dynamic rupture on a bimaterial interface governed by slip-weakening friction: Geophysical Journal International, v. 165, p. 469-484.

Valoroso, L., L. Chiaraluce, and C. Collettini, 2014, Earthquakes and fault zone structure: Geology, v. 42, p. 343-346.

Wilson, J. E., J. E. Chester, and F. M. Chester, 2003, Microfracture analysis of fault growth and wear processes, Punchbowl Fault, San Andreas system, California: Journal of Structural Geology, v. 25, p. 1855-1873.

Xu, S., Y. Ben-Zion, and J. P. Ampuero, 2012b, Properties of inelastic yielding zones generated by in-plane dynamic ruptures-II. Detailed parameter-space study: Geophysical Journal International, v. 191, no. 3, p. 1343-1360.

Walsh, J. J., and J. Watterson, 1987, Distributions of cumulative displacement and seismic slip on a single normal fault surface: Journal of Structural Geology, v. 9, p. 1039-1046.

Weng, H., H. Yang, Z. Zhang, and X. Chen, 2016, Earthquake rupture extents and coseismic slips promoted by damaged fault zones: Journal of Geophysical Research Solid Earth, v. 121, p. 4446-4457.

Zoback, M. D., S. Hickman, and W. Ellsworth, 2011, Scientific drilling into the San Andreas Fault Zone - An overview of SAFOD's first five years: Scientific Drilling, v. 11, p. 14-28.

Author Vitae

Zonghu Liao received a M.S. and a Ph.D. in structural geology from the University of Oklahoma. Currently, he serves as associate professor within the China University of Petroleum, Beijing. His research interests include seismic interpretation, faulting mechanisms, and the landslides.

Hui Liu received a Bachelor in Geophysics from Jilin University, China and a M.S. from China University of Petroleum, Beijing. His research interests include seismic interpretation, and artificial intelligent.

Brett Carpenter received his M.S. and Ph.D. in geosciences from Pennsylvania State University. Currently he serves as Assistant Professor of Geology and Geophysics at the University of Oklahoma, Norman. His research interests focus on how fault structure and small-scale processes affect large scale fault and crustal behavior. He is particularly interested in the behavior of earth materials at shallow to central crustal conditions, where destructive earthquakes originate and propagate.

Kurt J. Marfurt joined The University of Oklahoma in 2007 where he serves as the Frank and Henrietta Schultz Professor of Geophysics within the ConocoPhillips School of Geology and

Geophysics. Marfurt's primary research interest is in the development and calibration of new seismic attributes to aid in seismic processing, seismic interpretation, and reservoir characterization. Marfurt earned a Ph.D. in applied geophysics at Columbia University's Henry Krumb School of Mines in New York in 1978 where he also taught as an Assistant Professor for four years. He worked 18 years in a wide range of research projects at Amoco's Tulsa Research Center after which he joined the University of Houston for 8 years as a Professor of Geophysics and the Director of the Allied Geophysics Lab. Marfurt leads short courses on attributes for SEG and AAPG and currently serves as Editor-in-Chief of the AAPG/SEG journal Interpretation.

Ze'ev Reches received a B.S. and an M.S. in geology from Hebrew University, Israel, and a Ph.D. in structural geology from Stanford University. He is now professor emeritus of structural geology at the University of Oklahoma. His prior work includes positions at Arizona State University, Stanford University, and the U.S. Geological Survey at Menlo Park, California, and Hebrew University, Israel. His research interests include earthquake and fault processes and rock mechanics.

Figure captions:

Figure 1. Schematic diagram showing the fault zone architectural components for a strike slip fault (after Caine et al., 1996). Red indicates fault core, grey for damage-zones, and the protolith is removed.

Figure 2. Density of fault damage as a function of fault normal distance from the fault center: a) Joint density versus fault normal distance by Sagy et al. (2001), FSR=Fracture-Spacing-Ratio; b) Fracture density versus fault normal distance (data number #DP10) by Wilson et al. (2003); c) Seismic events versus fault normal distance by Powers and Jordan (2010); d) and schematic diagram shows the decay relationship between inferred damage parameter versus fault normal distance. Note a and b are coefficients of $D = \mathrm{a}\ e^{-\mathrm{b}x}$.

Figure 3. a) Two-way travel time (TWT) map of the top of the Woodford Shale indicating its large-scale structure of gently dipping (<2°) to the southwest. The time structural is co-rendered with the 3D determined coherence of a horizontal surface at this depth. The dark lineaments (Interpreted R faults are marked by red dash lines in the zoom-in figure in the right) reveal structural elements, including the north-south El Reno fault zone within the red rectangle. Note transparent color is used for high coherence area. General location of the study area in the Anadarko Basin, Oklahoma (red star in Oklahoma). b) Seismic amplitude map co-rendered with the coherence along the top of the Woodford Shale. Index (C1, C11) show lines of sampling numbered S to N, with 1520m (~ 5000 ft) in space.

Figure 4. Seismic amplitude and coherence across section maps normal to the El Reno fault in the study area. a) and b) are amplitude maps of section C2 and C8 respectively (showed in Figure 3), red rectangles indicate the fault area corresponding to the area of low coherence value in c) and d).

Figure 5. Profiles of the coherence values across El Reno fault at the Woodford Shale level. Profiles locations in Fig. 3. Note the inverse scale of the coherence. Zones of coherence values below background coherence are interpreted as damage-zones. Coherence reduction intensity shown in colors: Pink- intense; grey- gentle; white- background. a) Damage-zones along the type 1 segment of El Reno fault characterized by Riedel shear sub-faults (C1-C7 sections in Fig. 3b). b) Damage-zones along the type 2 segment of El Reno fault characterized by a pull-apart basin (C6-C11 sections in Fig. 3b).

Figure 6. Profiles of the root mean square (RMS) amplitude values across El Reno fault at the Woodford Shale level. Profiles locations in Fig. 3. Zones of abnormal low values are interpreted as damage-zones. a) Damage-zones along the type 1 segment of El Reno fault (C1-

C7 sections in Fig. 3b). b) Damage-zones along the type 2 segment of El Reno fault (C6-C11 sections in Fig. 3b).

Figure 7. Coherence damage-zones variations with depth intervals from 1800ms to 2500ms. a) Type 1 segment with Riedel shear sub-faults). b) Type 2 segment with pull-apart basin. The zone of low coherence values below background coherence indicates the damage-zone (colored in grey).

Figure 8. a) Normalized damage density (fractures or seismic events) as a function of normalized distance from the fault zone. Three examples from references (Sagy et al., 2001; Wilson et al., 2003; Powers and Jordan, 2010). All data are well fit by the model $D = \mathrm{a}\ e^{-\mathrm{b}x}$ where coefficients a and b are determined by different fault lithology and geometry. b) Normalized coherence (average of C1-C7) as a function of normalized distance from the fault zone for right block and c) left block of type 1 segment of El Reno fault with Riedel shear sub-faults (shown by the two arrows). d) Normalized coherence (average of C6-C11) as a function of normalized distance from the fault zone for right block with fault wall of type 2 segment of El Reno fault with pull-apart basin and e) left block in ERF.

Figure 9. Schematic presentation of the fault model with (a) heterogeneous stress field over a scaling region (Dieterich and Smith, 2009; Powers and Jordan, 2010) (a), and the associated damage-zones (Chester 2005) (b).

Figure 1:

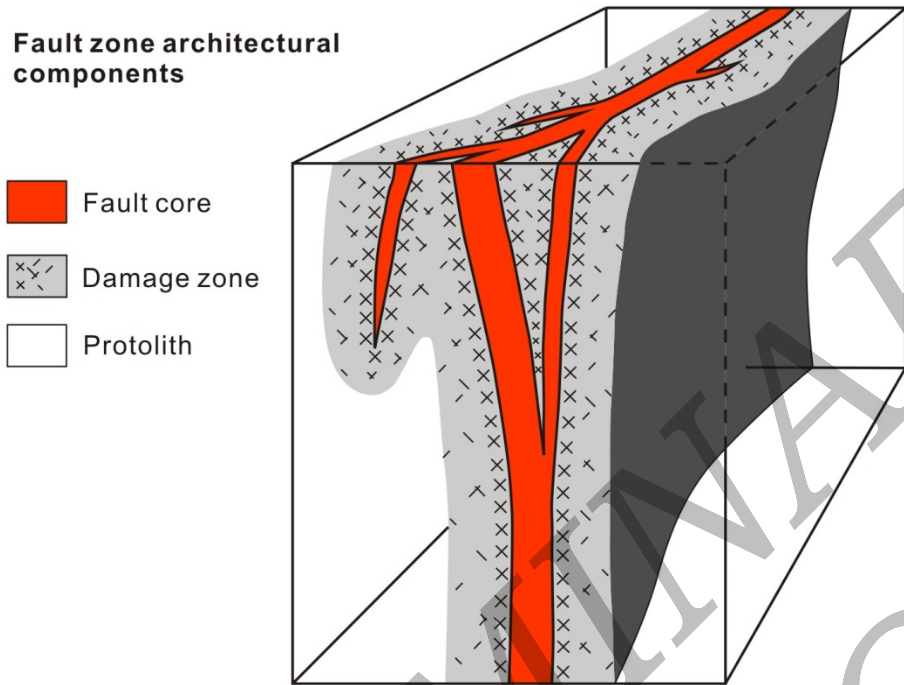
Fault zone architectural components
Fault core
Damage zone
Protolith

Figure 2:

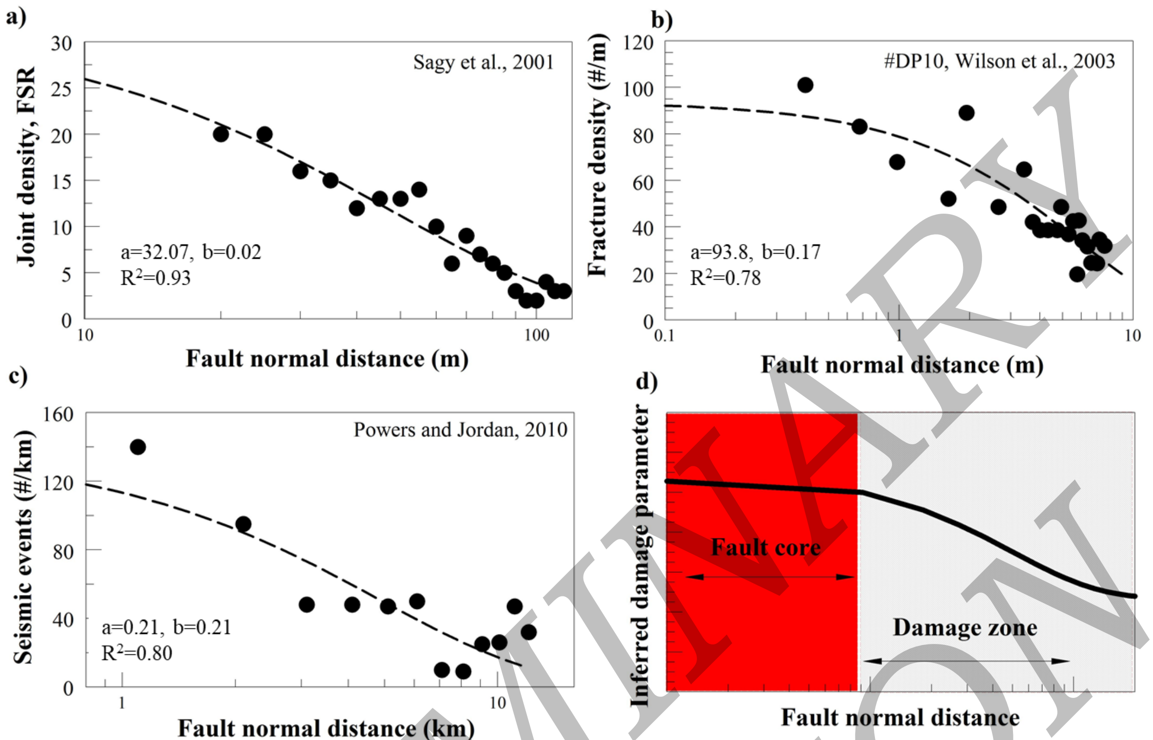

a)
Sagy et al., 2001
Joint density, FSR
a=32.07, b=0.02
R²=0.93
Fault normal distance (m)
b)
#DP10, Wilson et al., 2003
Fracture density (#/m)
a=93.8, b=0.17
R²=0.78
Fault normal distance (m)
c)
Powers and Jordan, 2010
Seismic events (#/km)
a=0.21, b=0.21
R²=0.80
Fault normal distance (km)
d)
Inferred damage parameter
Fault core
Damage zone
Fault normal distance

Figure 3:

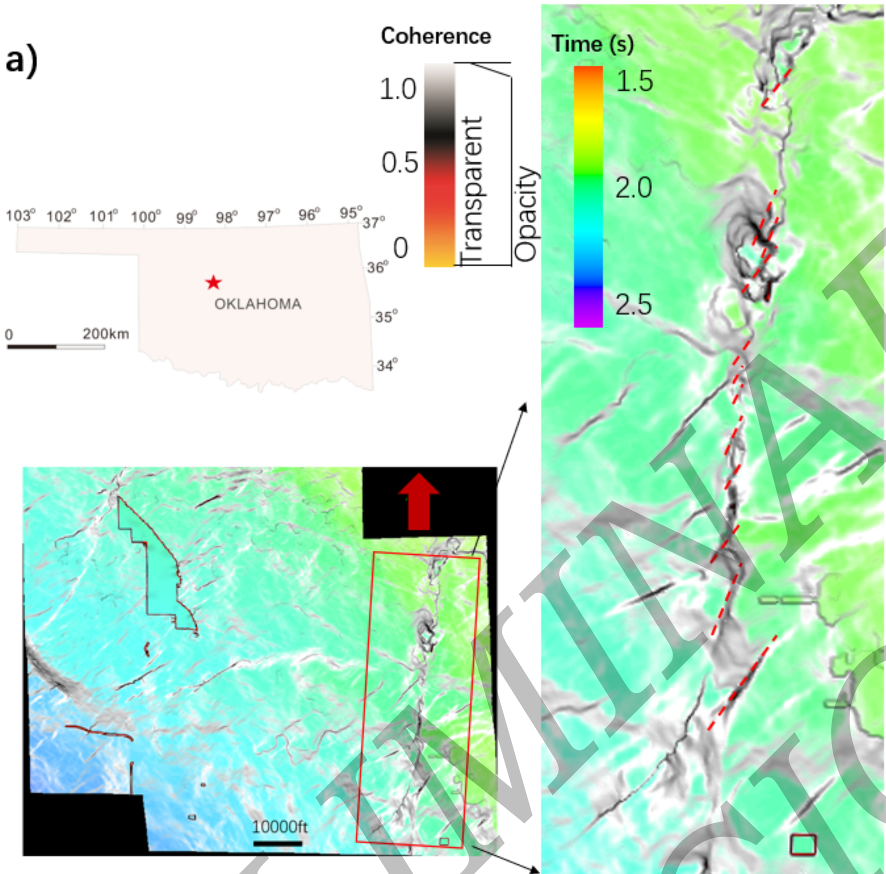

a)
Coherence
1.0
0.5
0
Transparent
Opacity
Time (s)
1.5
2.0
2.5
103° 102° 101° 100° 99° 98° 97° 96° 95°
37° 36° 35° 34°
OKLAHOMA
0
200km
10000ft

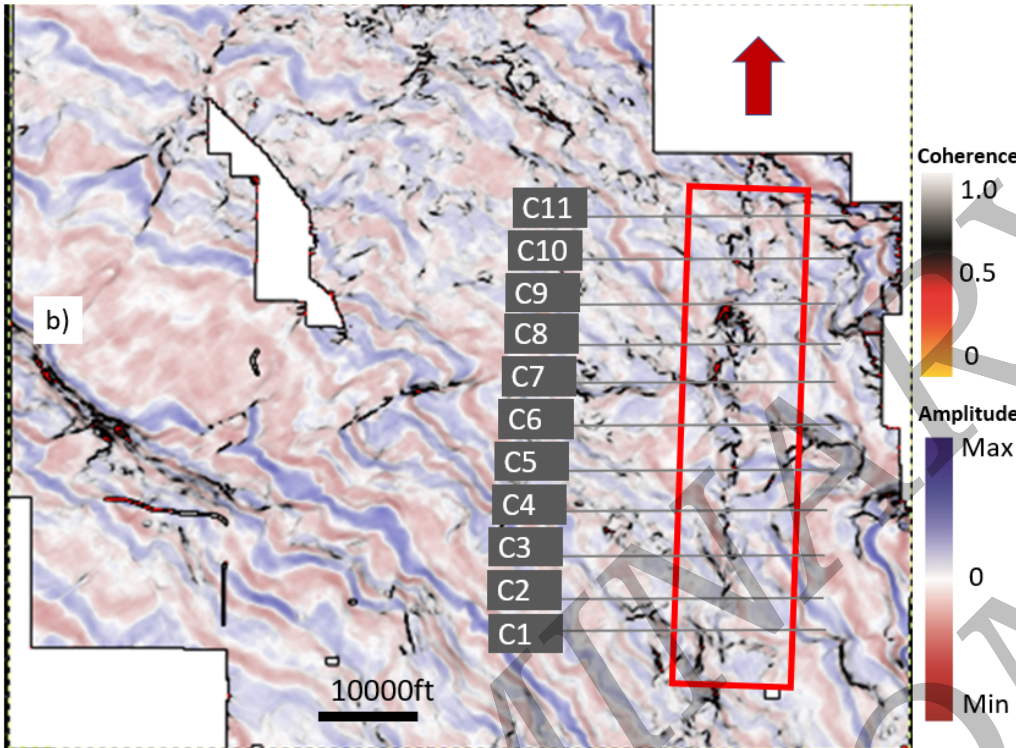
b)
C11
C10
C9
C8
C7
C6
C5
C4
C3
C2
C1
10000ft
Coherence
1.0
0.5
0
Amplitude
Max
0
Min

Figure 4

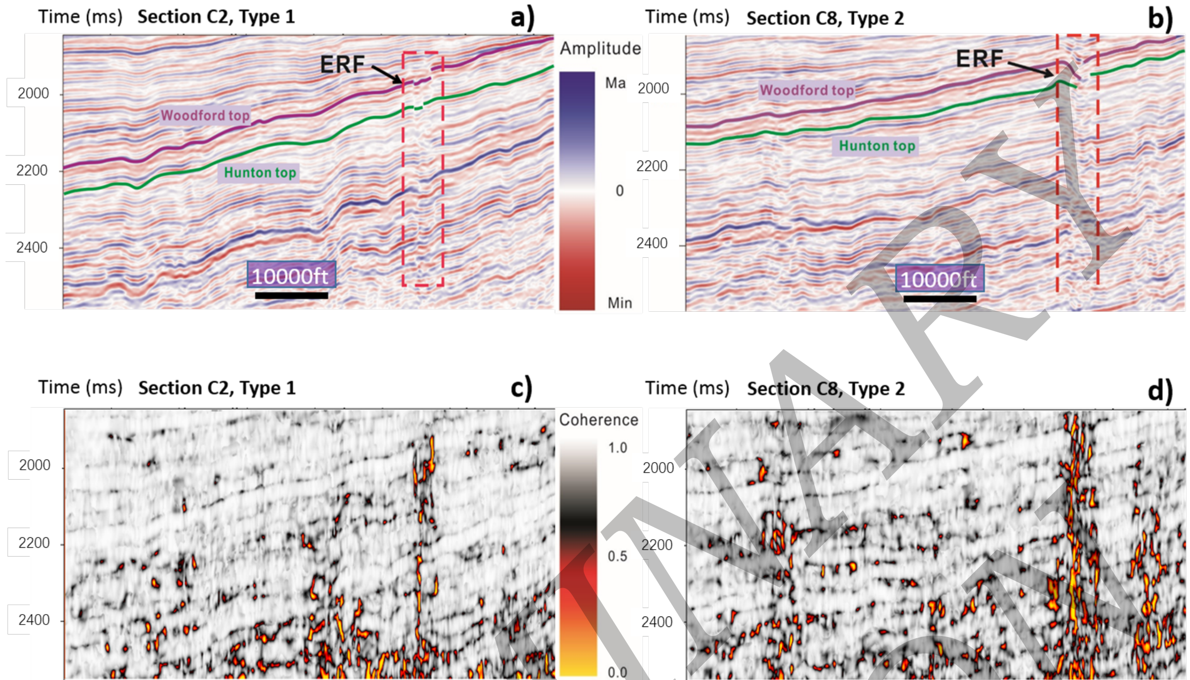

Time (ms)
Section C2, Type 1
a)
ERF
Woodford top
Hunton top
2000
2200
2400
10000ft
Amplitude
Ma
0
Min
Time (ms)
Section C8, Type 2
b)
ERF
Woodford top
Hunton top
2000
2200
2400
10000ft
Time (ms)
Section C2, Type 1
c)
2000
2200
2400
Coherence
1.0
0.5
0.0
Time (ms)
Section C8, Type 2
d)
2000
2200
2400

Figure 5:

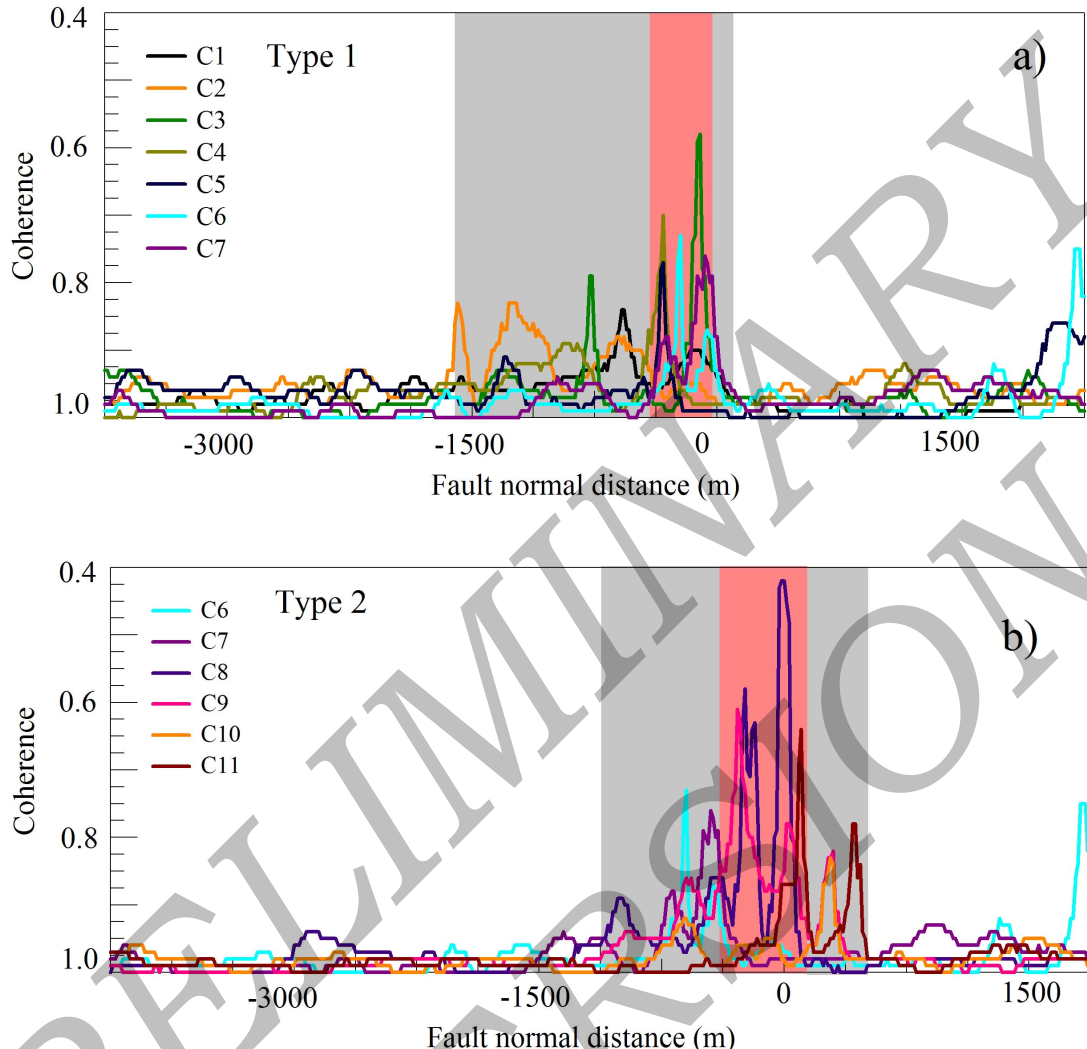

Figure 6

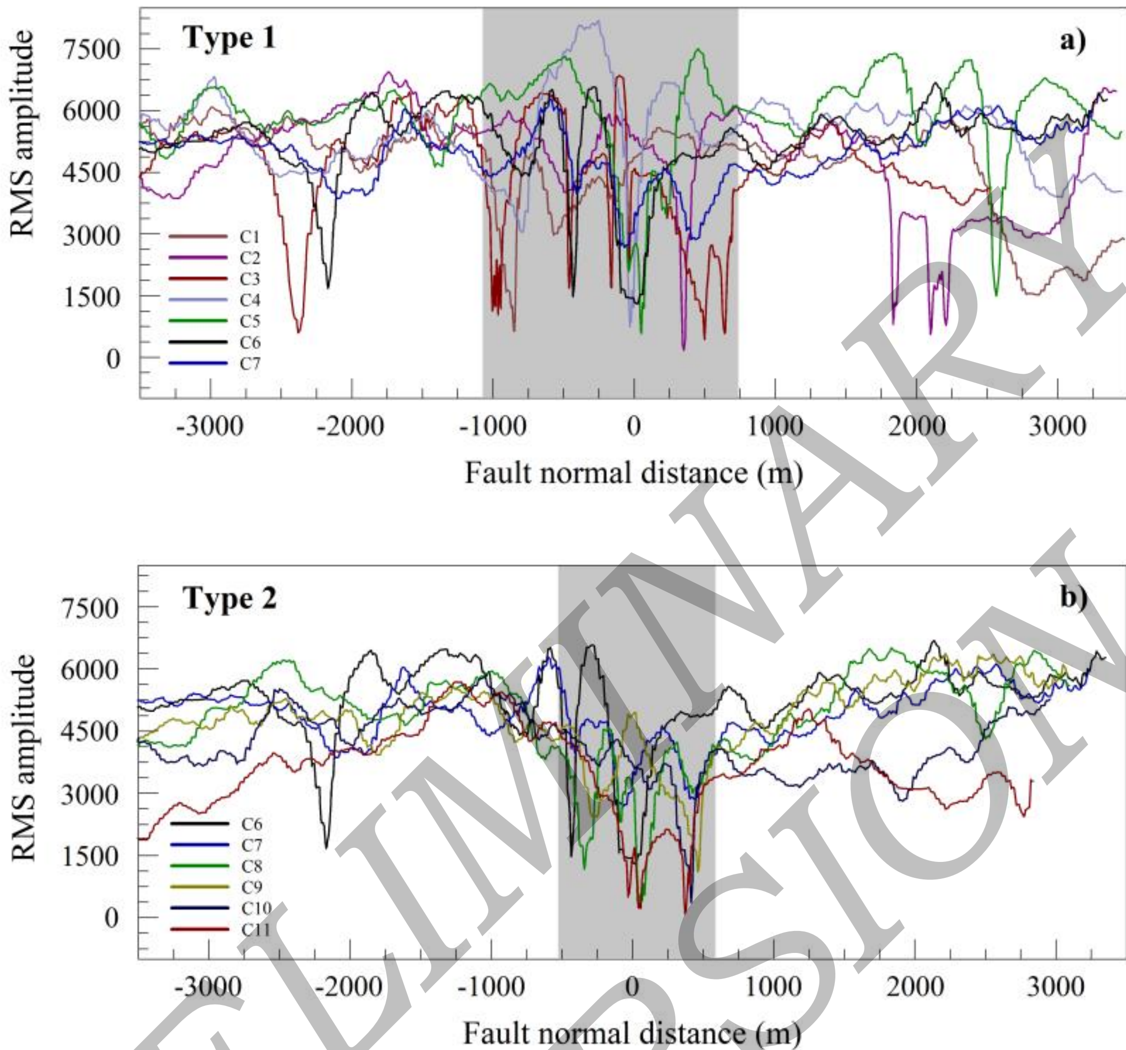
Type 1
a)
RMS amplitude
7500
6000
4500
3000
1500
0
C1
C2
C3
C4
C5
C6
C7
-3000
-2000
-1000
0
1000
2000
3000
Fault normal distance (m)
Type 2
b)
RMS amplitude
7500
6000
4500
3000
1500
0
C6
C7
C8
C9
C10
C11
-3000
-2000
-1000
0
1000
2000
3000
Fault normal distance (m)

Figure 7:

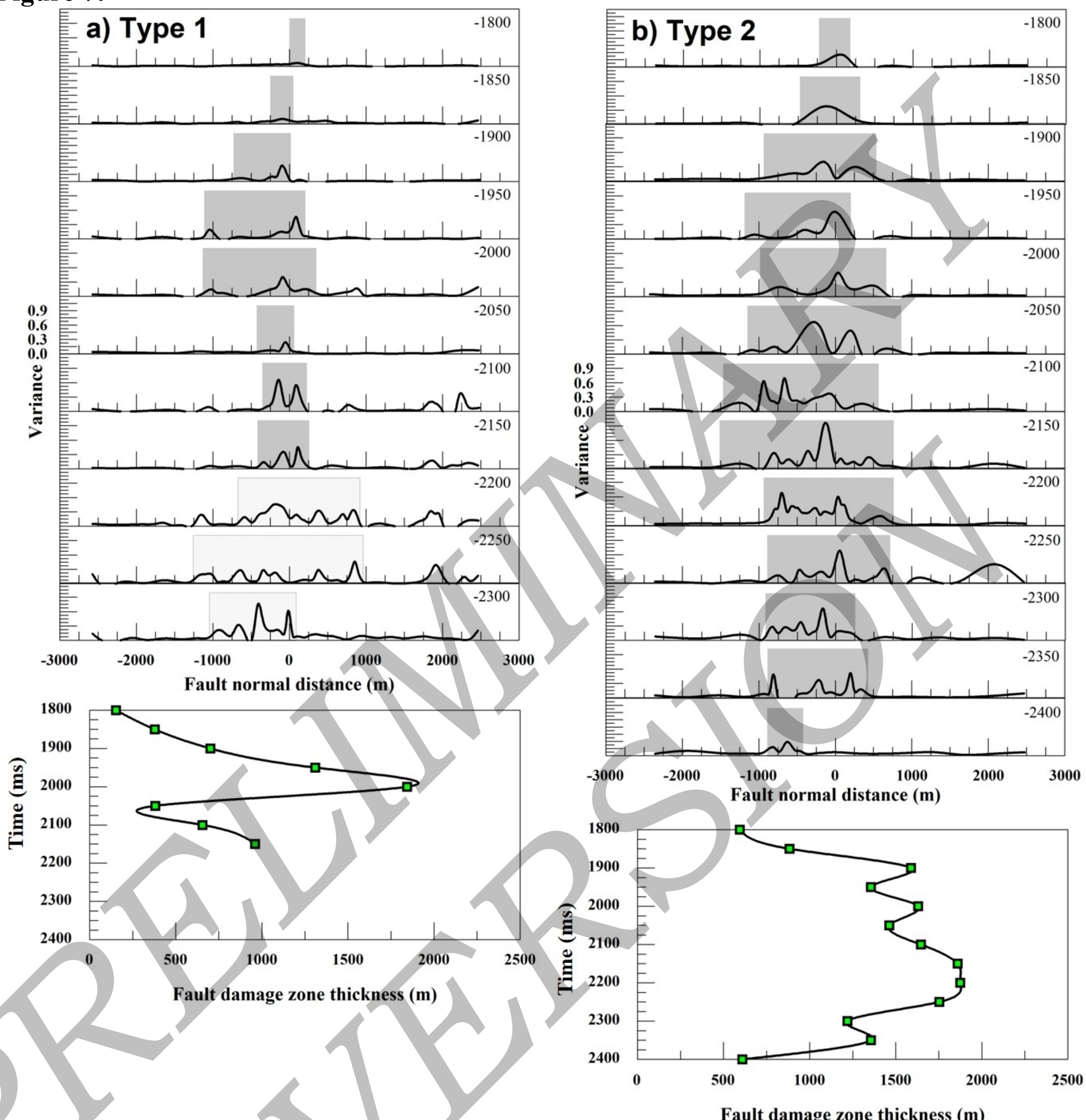

a) Type 1
b) Type 2
-1800
-1850
-1900
-1950
-2000
-2050
-2100
-2150
-2200
-2250
-2300
-2350
-2400
0.9
0.6
0.3
0.0
Variance
-3000
-2000
-1000
0
1000
2000
3000
Fault normal distance (m)
1800
1900
2000
2100
2200
2300
2400
Time (ms)
0
500
1000
1500
2000
2500
Fault damage zone thickness (m)

555 Figure 8:

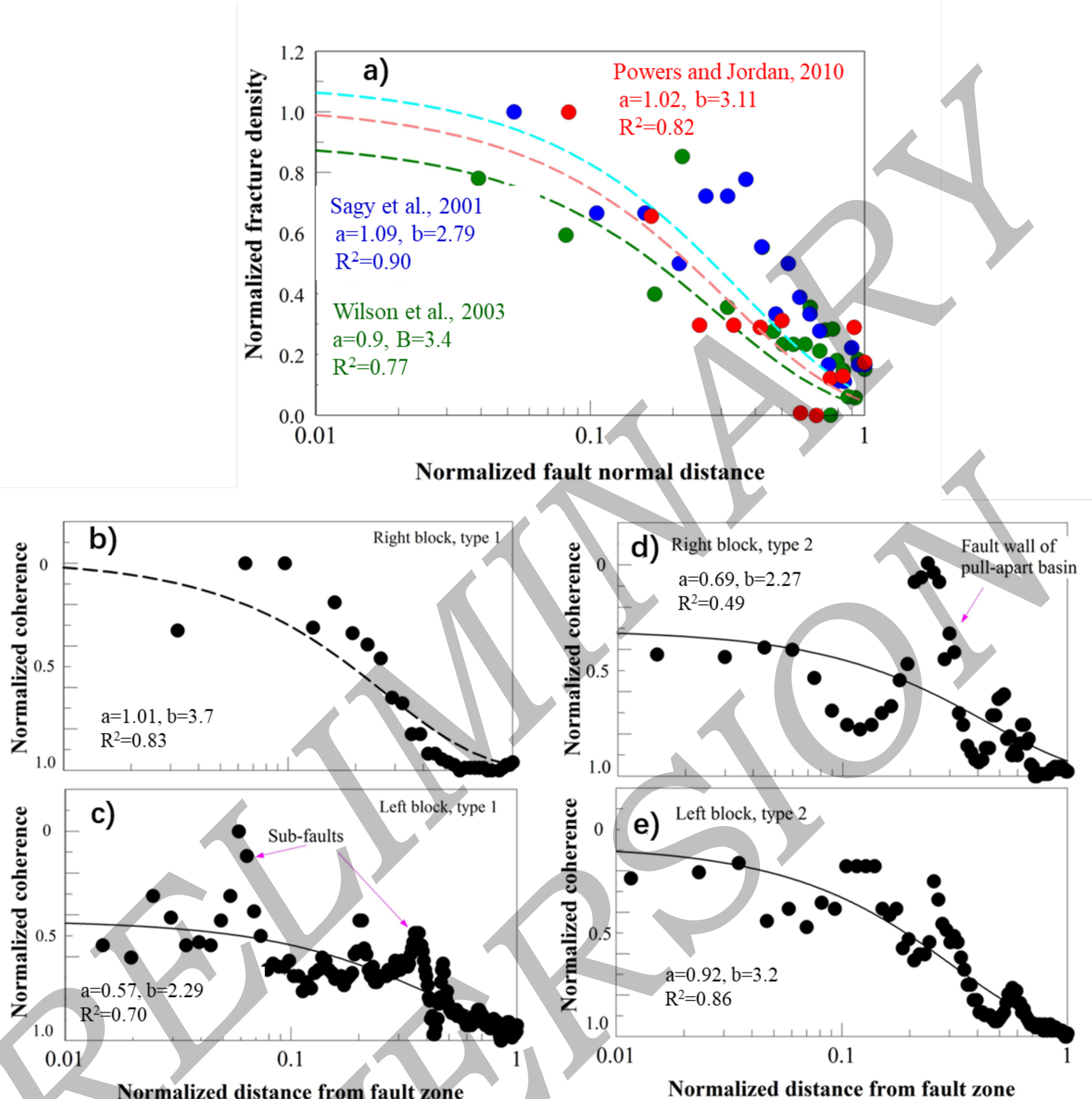

556

557

Figure 9:

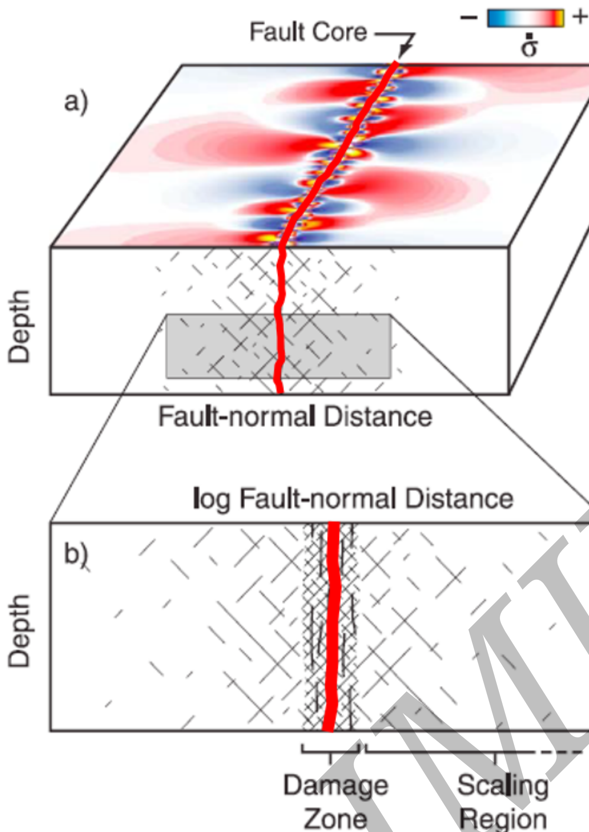
Fault Core
a)
Depth
Fault-normal Distance
log Fault-normal Distance
b)
Depth
Damage
Zone
Scaling
Region